Supplementary Information

Thermodynamically stable low-Na O3 cathode materials driven by intrinsically high ionic potential discrepancy

Meng Li[1,2+], Haoxiang Zhuo[3,9+], Yang Xu[1,4], Qihang Jing[1,2], Yanlong Wu[3], Yang Gu[1], Zhou Liao[1,5], Kuan Wang[1], Miao Song[6], Xiaona Li[5], Jianwen Liang[1], Changtai Zhao[1], Yingying Jiang[1], Tianci Wu[2], Dongsheng Geng[2,7*], Jiangtao Hu[8*], Xueliang Sun[5*], Biwei Xiao[1,3,9*]

1. GRINM (Guangdong) Research Institute for Advanced Materials and Technology, Foshan, Guangdong, 528051, P.R.China
2. University of Science and Technology Beijing, Beijing, 100083, China
3. China Automotive Battery Research Institute Co., Ltd., Beijing, 100088, P.R.China
4. School of Materials Science and Engineering, Hubei University, Wuhan 430062, P.R. China
5. Eastern Institute for Advanced Study, Eastern Institute of Technology, Ningbo, Zhejiang 315200, P.R.China
6. Powder Metallurgy Research Institute, Central South University, Changsha, Hunan 410083, P.R.China
7. Nanjing University of Information Science & Technology, Nanjing, Jiangsu 210044, P.R.China
8. Graphene Composite Research Center, College of Chemistry and Environmental Engineering, Shenzhen University, Shenzhen, 518060, China
9. General Research Institute for Nonferrous Metals, Beijing, 100088, P.R.China

+ These authors contributed equally to this work.

Experimental Section

Materials Synthesis.

The $Na_{0.67}Mn_{0.7-x-y-z}Ni_{0.3}Li_xFe_yTi_zO_2$ (x+y+z=0.3) materials were synthesized by mixing desired amount of sodium carbonate anhydrous (99.5%), Li_2CO_3 (99.99%), Mn_2O_3 (98%), nano-NiO (99.5%), Fe_2O_3 (99%) and TiO_2 (99%) thoroughly using planetary ball milling for 10 h at 500 rpm. Afterwards, the mixture was pressed into pellets and annealed in a tube furnace under air. The solid-state synthesis follows a two-step process, first, the furnace was heated to 500℃ with a ramping rate of 3℃/min and kept isothermal for 2 h. Then, the furnace temperature was increased to 950℃ at the same ramping rate of 3℃/min and kept for 10 h. Afterwards, the furnace was cooled down to room temperature with a rate of 5℃/min. Before testing, they were ground thoroughly to crush the large chunks of particles. For the study of dopant effects, Co_2O_3 (99%), CuO (99%), ZnO (99%), MgO (98%), Sb_2O_5(99%) and Nb_2O_5 (99%) were used as the dopant sources, mixed according to the target components and processed consistently with the above steps.

1.5NaCl-$(LaCl_3.CeCl_3.ZrCl_4.HfCl_4.TaCl_5)_{0.2}$//$Na_3PS_4$//$Na_{15}Sn_4$ synthesis process:[1] All preparation processes and sample treatments were carried out in an Ar-filled glovebox (O_2 < 1 ppm, H_2O < 1 ppm). The UCl_3-type halides HCF-Sm/HCF-La and ternary halides $NaTaCl_6$, Na_2ZrCl_6, and Na_2HfCl_6 were synthesized by ball-milling the starting materials of NaCl (99.9%), $SmCl_3$ (99.9%) and $LaCl_3$ (99.8%), $TaCl_5$ (99.99%), $ZrCl_4$ (99.9%), and $HfCl_4$ (99.9%) at the stated stoichiometric ratio. For ball-milling synthesis, the mixture of precursors was sealed in a zirconia jar (100 mL) under vacuum and ball milled at 500 rpm for 60 cycles. Each cycle included 10-min milling and 5-min resting. The heterogeneous composite was synthesized by ball-milling as-prepared HCF-Sm/HCF-La and $NaTaCl_6$/Na_2ZrCl_6/Na_2HfCl_6 at 500 rpm for another 20 cycles or directly from the precursors at 500 rpm for 90 cycles. Na_3PS_4 was synthesized by mechanical ball milling using a high energy ball mill. Na_2S (99%) and P_2S_5 (99%) were proportionally milled in an 80 mL ZrO_2 ball mill jar at 500 r.p.m. for 10 hours. The ball milled product was extracted from the jars in a glove box, pelletized at 3T, and loaded into vacuum quartz tubes. Na_3PS_4 was annealed at 270°C for 2 h at a ramp rate of 5°C/min. The Na_3PS_4 obtained was extracted from the quartz tubes and then hand ground into powder for future use. The $Na_{15}Sn_4$ anode was prepared by mixing stoichiometric amounts of Na and Sn.

Materials Characterizations

X-ray diffraction (XRD): The powder XRD patterns were collected using a Rigaku Miniflex II XRD with Cu Kα radiation (λ = 1.5418 Å). Regular tests were conducted at a scan rate of 5°/min from 10° to 90°, the samples for Rietveld Refinements were measured at a scan rate of 1°/min from 10° to 90°.

In-situ XRD: The charge/discharge crystal structure information was collected using a designed in situ mold cell. The mold battery with holes for beam pass were used to make the in-situ cell. The hole at the top cases of the mold battery were sealed with Kapton tape after cell assembly. The electrode had a mass loading of 11 mg/cm^2, the in-situ cell was rested for 3 h before doing in-situ XRD. During the in-situ experiment, LANHE Battery Tester was used to discharge/charge the cell using a constant rate of 24 mA/g between 2.0 and 4.2 V. In-situ high-temperature XRD: The data acquisition temperature node of MN are 30 ℃, 200 ℃ , 300 ℃, 400 ℃, 450 ℃, 500 ℃, 525 ℃, 550 ℃, 575 ℃,600 ℃, 625 ℃, 650 ℃, 675 ℃, 700 ℃, 725 ℃, 750 ℃, 775 ℃, 800 ℃, 825 ℃, 850 ℃, 875 ℃, 900 ℃, 930 ℃, 940 ℃, 950 ℃. MNLT is the same as MN with one more node at 920°C, the temperature ramp rate is 3℃/min.

Scanning electron microscope (SEM): SEM images were taken using ZEISS SUPRA55 scanning electron microscopy operating at 10 kV.

Scanning transmission electron microscopy (STEM): For the microstructure analysis, an aberration-corrected TEM (Spectra 300, Thermo Fisher Scientific, USA) equipped with a high-angle annular dark-field (HAADF)

detector and an EDS system was employed at 300 kV for HAADF-STEM imaging and atomic scale composition analysis. The electrons from 55 to 200 mrad were collected for HAADF-STEM imaging.

Differential Scanning Calorimeter (DSC): The thermal behavior of desodiated cathodes in the electrolyte was investigated by DSC (METTLER TOLEDE TGA/DSC 3^{+}).

X-ray photoelectron spectroscopy (XPS): PHI 5000 Versa Probe was used to analyze the chemical states of the chemical compositions.

Electrochemical measurements

The electrode was made by mixing the active material, Acetylene black and polyvinylidene fluoride (PVDF) with a ratio of 85:7:8 dispersed in N-methyl-2-pyrrolidone (99%, Alfa Aesar) using a Thinky ARE350 mixer. The slurry was pasted onto Al foil and dried under 80°C in a vacuum oven overnight. The active material loading was controlled to be around 8 mg/cm^2. The electrodes were assembled in CR2032 coin cells in a glovebox filled with Argon gas. The O_2 and H_2O levels are below 1 ppm. Na metal was used as the counter electrode. The cells tested between 2-4.2 V or 2-4.3 V used 160 µL electrolyte (1M $NaClO_4$ in PC=100 Vol% with 5% FEC). The coin cells were tested using an LANHE Battery Tester at desired rates in room temperature. For the galvanostatic intermittent titration technique (GITT) measurements, the cells were charged at a current density of 0.1C (1C=120 mA/g) for 15 min, followed by open circuit relaxation for 120 min.

Pouch Cell Parameters: The electrode was made by mixing the MNFLT/NFM333, Acetylene black and polyvinylidene fluoride (PVDF) with a ratio of 92:6:2. For the anode side: Hard carbon, Acetylene black and polyvinylidene fluoride (PVDF) with a ratio of 93:3:4, N/P ratio is controlled at 1.1. The pouch cell tested between 1-4.1 V.

All-solid-state battery assembly based on previous work:[1] the mold pressurized battery was assembled by using the MNFLT as the cathode, $Na_{15}Sn_4$ as the negative electrode, 1.5NaCl-$(LaCl_3.CeCl_3.ZrCl_4.HfCl_4.TaCl_5)_{0.2}$ and Na_3PS_4 as the separator. A total of 100 mg of the electrolyte powder to be tested was pressed at≈200 MPa to form an SE layer. The cathode composite (MNFLT: 1.5NaCl-$(LaCl_3.CeCl_3.ZrCl_4.HfCl_4.TaCl_5)_{0.2}$: carbon black (CB) = 70:30:1) was uniformly spread onto the surface of one side of the electrolyte layer and pressed with ≈500 MPa for 1 min. Then about 7 mg of the cathode composite was placed on one side of the 1.5NaCl-$(LaCl_3.CeCl_3.ZrCl_4.HfCl_4.TaCl_5)_{0.2}$ pellet and pressed at the same pressure, and on the opposite side of 1.5NaCl-$(LaCl_3.CeCl_3.ZrCl_4.HfCl_4.TaCl_5)_{0.2}$, the Na_3PS_4, and an excess of $Na_{15}Sn_4$ alloy (20 mg) were pressed in order.

DFT Calculation

All of the First-principle calculations were performed by Vienna ab initio simulation package (VASP) with the projector augmented wave (PAW) method based on the Density Functional Theory (DFT).[2] The strong correlation effect of Mn, Ni and Ti has been modified by the DFT with Hubbard U correction,[3] and the values of U-J for Mn, Ni, Ti ions are set to be 3.9, 6.2 and 1.5, respectively. The calculations were performed by the spin-polarized generalized gradient approximation (GGA) with the Perdew−Burke–Ernzerho (PBE) exchange−correlation functional. The cutoff energy was set to be 520 eV. The total energy converged was set to be 10^{-5} eV and the final force on each atom is less than 0.05 eV/Å. The Monkhorst–Pack scheme was selected in the Brillouin zone.

Cationic potential calculations

$\Phi = \frac{\Phi TM * \Phi Na}{\Phi O}$, Φ=Charge/ionic radius (nm), where ΦTM represents the weighted average ionic potential of TMs, ΦNa represents the weighted average ionic potential of Na, ΦO=28.57.[4]

Supplementary Tables

Table S1. Stoichiometry from inductively coupled plasma of MNLT, MNFL, MNFLT.

Smple		
$Na_{0.67}Mn_{0.4}Ni_{0.3}Li_{0.15}Ti_{0.15}O_2$ (MNLT)	n_{Na}: n_{Mn}: n_{Ni}: n_{Li}: n_{Ti}	0.658:0.398:0.296:0.143:0.156
$Na_{0.67}Mn_{0.4}Ni_{0.3}Fe_{0.15}Li_{0.15}O_2$ (MNFL)	n_{Na}: n_{Mn}: n_{Ni}: n_{Fe}: n_{Li}	0.667:0.392:0.298:0.153:0.141
$Na_{0.67}Mn_{0.4}Ni_{0.3}Fe_{0.15}Li_{0.1}Ti_{0.05}O_2$ (MNFLT)	n_{Na}: n_{Mn}: n_{Ni}: n_{Fe}: n_{Li}: n_{Ti}	0.662:0.395:0.291:0.147:0.094:0.0493

Table S2. The summary of lattice parameters (Å), interlayer distances (Å) of d(O-Na-O) and d(O-Me-O) and their ratio for the typical P2- and O3- phase compounds.

	Number	Compound	$d_{(o\text{-}Na\text{-}o)}$/Å	$d_{(o\text{-}Me\text{-}o)}$/Å	Ratio of $d_{(O\text{-}Na\text{-}O)}$ to $d_{(O\text{-}Me\text{-}O)}$	Ref
P2 Phase	1	$Na_{0.51}Mn_{0.93}O_2$	3.8810	1.7015	2.28093	5
	2	$Na_{0.67}CoO_2$	3.4865	1.9679	1.77164	6
	3	$Na_{0.67}Ni_{0.33}Mn_{0.67}O_2$	3.4804	2.0971	1.65963	7
	4	$Na_{0.628}Fe_{0.03}Co_{0.97}O_2$	3.5032	1.9678	1.78026	8
	5	$Na_{0.74}Ni_{0.58}Sb_{0.42}O_2$	3.5071	2.1061	1.66521	9
	6	$Na_{0.67}Ni_{0.33}Ti_{0.67}O_2$	3.4680	2.1021	1.64986	10
	7	$Na_{0.67}Co_{0.33}Ti_{0.67}O_2$	3.5534	2.0316	1.74906	11
	8	$Na_{0.66}Li_{0.22}Ti_{0.78}O_2$	3.4736	2.0899	1.66209	12
	9	$Na_{0.67}Mg_{0.25}Mn_{0.75}O_2$	3.8141	1.7949	2.12497	7
	10	$Na_{0.67}Mn_{0.33}Fe_{0.33}Co_{0.34}O_2$	3.5584	2.0016	1.77778	13
O3 Phase	1	$NaCo_{0.5}Fe_{0.5}O_2$	3.23820	2.2445	1.44268	14
	2	$NaTiO_2$	3.2051	2.2157	1.44650	15
	3	$NaCrO_2$	3.2173	2.1005	1.53167	16
	4	$NaFeO_2$	3.2670	2.0538	1.59070	17
	5	$NaCoO_2$	3.1886	2.0046	1.59062	18
	6	$NaNi_{0.5}Mn_{0.5}O_2$	3.2486	2.0861	1.55724	19
	7	$Na_{0.90}Ni_{0.45}Ti_{0.55}O_2$	3.2323	2.1585	1.49747	10
	8	$NaNi_{0.33}Co_{0.33}Fe_{0.34}O_2$	3.1592	2.1255	1.48633	20
	9	$NaNi_{0.25}Fe_{0.5}Mn_{0.25}O_2$	3.0165	2.3130	1.30414	21
	10	$Na_{0.66}Mg_{0.34}Ti_{0.66}O_2$	3.3497	2.1166	1.58259	22
This	11	$Na_{0.67}Mn_{0.7}Ni_{0.3}O_2$ (MN)	3.568 (P2)	2.005	1.779	
	12	$Na_{0.67}Mn_{0.4}Ni_{0.3}Fe_{0.3}O_2$ (O3/P2) (MNF)	3.399/3.563 (O3/P2)	2.038/2.032 (O3/P2)	1.668/1.753 (O3/P2)	
	13	$Na_{0.67}Mn_{0.4}Ni_{0.3}Ti_{0.3}O_2$ (MNT)	3.558	2.015	1.766	
	14	$Na_{0.67}Mn_{0.4}Ni_{0.3}Fe_{0.15}Li_{0.15}O_2$ (MNFL)	3.369	1.989	1.694	

work	15	$Na_{0.67}Mn_{0.4}Ni_{0.3}Li_{0.15}Ti_{0.15}O_2$ (MNLT)	3.428	1.995	1.718	
	16	$Na_{0.67}Mn_{0.4}Ni_{0.3}Fe_{0.15}Ti_{0.15}O_2$ (O3/P2) (MNFT)	3.631/3.62 (O3/P2)	1.847/1.939 (O3/P2)	1.966/1.867 (O3/P2)	
	17	$Na_{0.67}Mn_{0.4}Ni_{0.3}Fe_{0.15}Li_{0.1}Ti_{0.05}O_2$ (MNFLT)	3.498	1.9	1.841	
	18	$Na_{0.67}Mn_{0.45}Ni_{0.22}Fe_{0.13}Li_{0.1}Ti_{0.05}Co_{0.05}O_2$ (MNFLTC)	3.584	1.885	1.901	

Table S3. The date of sodium ion layer oxide cathode material pouch cell batteries.

Material	Specific capacity (mAh g^{-1})	capacity (Ah)	voltage window	energy density	Ref
VC-NFMO	95mAh/g (100mA/g)	2.94Ah	1-4.5 V	120Wh/kg	[23]
VC-NFMO	95mAh/g (100mA/g)	5.53Ah	1-4.5 V	170Wh/kg	[23]
NLFMO	198 mAh/g (10 mAg^{-1})	1.3Ah	1.5-4.3 V	165Wh/kg	[24]
KT-NFM	126.5 mAh/g (100 mAg^{-1})	0.6Ah	1.9-3.9 V	135.6 Wh/kg	[25]
ZT-NFM	125 mAh/g (100 mAg^{-1})	2.5Ah	1.7-3.9 V	133 Wh/kg	[26]
$NaNi_{0.5}Mn_{0.3}Co_{0.2}O_2$	101 mAh/g (100 mAg^{-1})	0.1Ah	1.5-4 V	＜30 Wh/kg	[27]
NMNCO-SL	111 mAh/g (120 mAg^{-1})	0.91Ah	1-3.9V	91.9 Wh/kg	[28]
MNFLT	126.5 mAh/g (120 mAg^{-1})	0.978 Ah	1-4.1V	125.6 Wh/kg	This work

Table S4. Positions of lithium ions and interstitial sites on the migration pathways

NFM333	x	y	z
Na1	0.000	0.000	0.500
i1	0.000	0.000	0.143

i2	0.500	0.750	0.518
s1	0.083	0.917	0.149
s2	0.417	0.813	0.815
s3	0.833	0.667	0.167
MNFLT	x	y	z
Na1	0.000	0.000	0.500
i1	0.667	0.333	0.185
s1	0.104	0.188	0.149
s2	0.833	0.167	0.167
s3	0.000	0.500	0.500
s4	0.500	0.500	0.500

Note: i represents the site, s represents the site saddle point. The optimal paths for NFM333 and MNFLT are Na1-s1-i1-s1-Na1.

Supplementary Figures

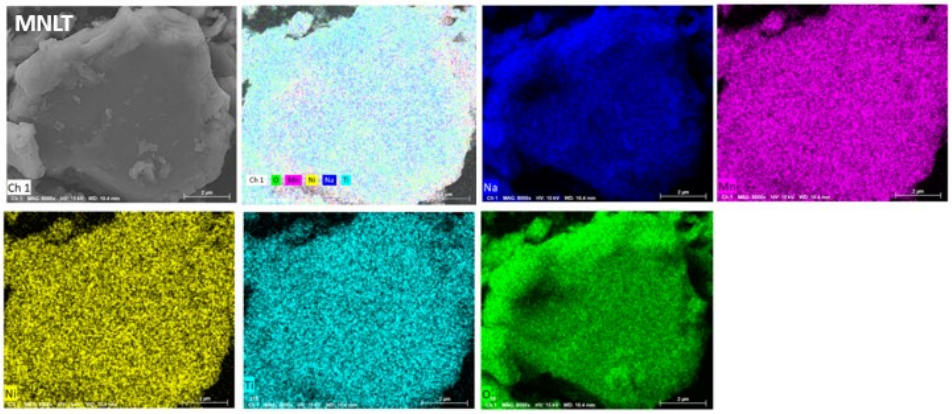

Fig. S1 SEM and elemental mapping images of MNLT.

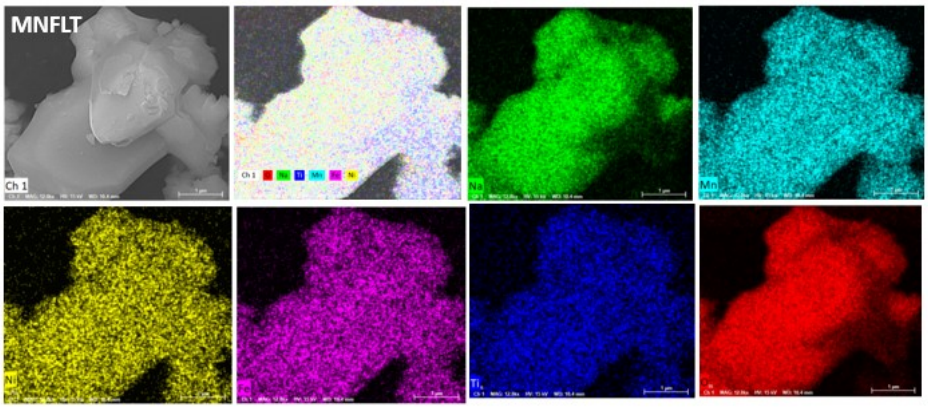

Fig. S2 SEM and elemental mapping images of MNFLT.

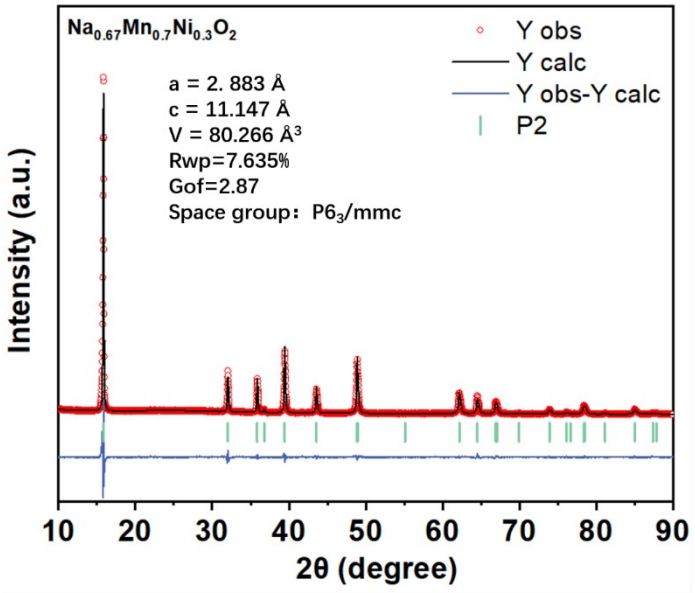

Fig. S3 XRD pattern and Rietveld refinement of $Na_{0.67}Mn_{0.7}Ni_{0.3}O_2$.

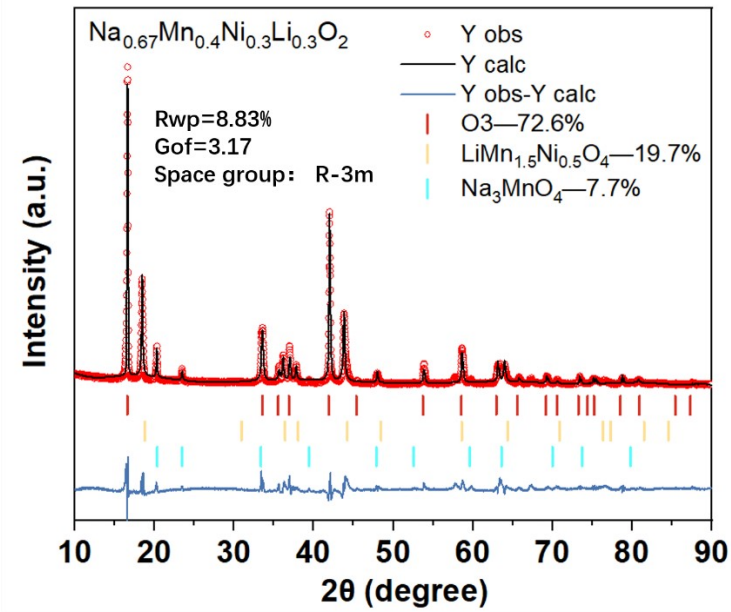

Fig. S4 XRD pattern of $Na_{0.67}Mn_{0.4}Ni_{0.3}Li_{0.3}O_2$, O3 phase mixed with $LiMn_{1.5}Ni_{0.5}O_4$ and Na_3MnO_4. The high Li content leads to a separate phase formation of Li and Na.

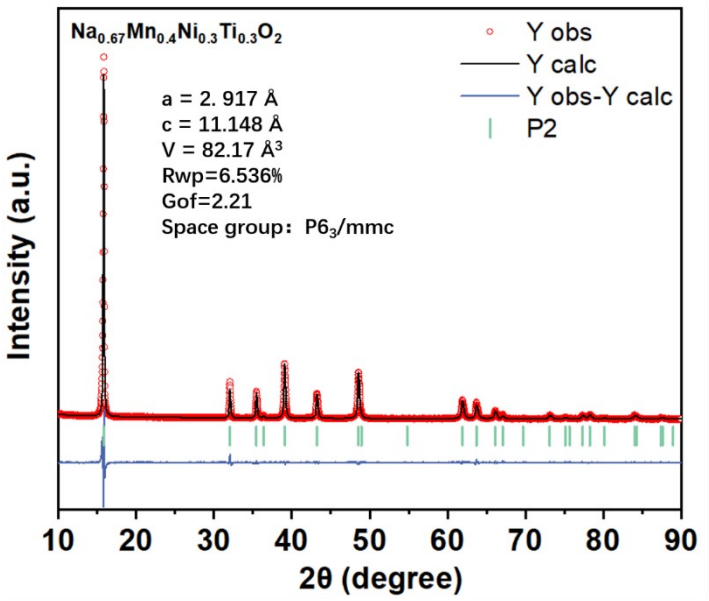

Fig. S5 XRD pattern and Rietveld refinement of $Na_{0.67}Mn_{0.4}Ni_{0.3}Ti_{0.3}O_2$.

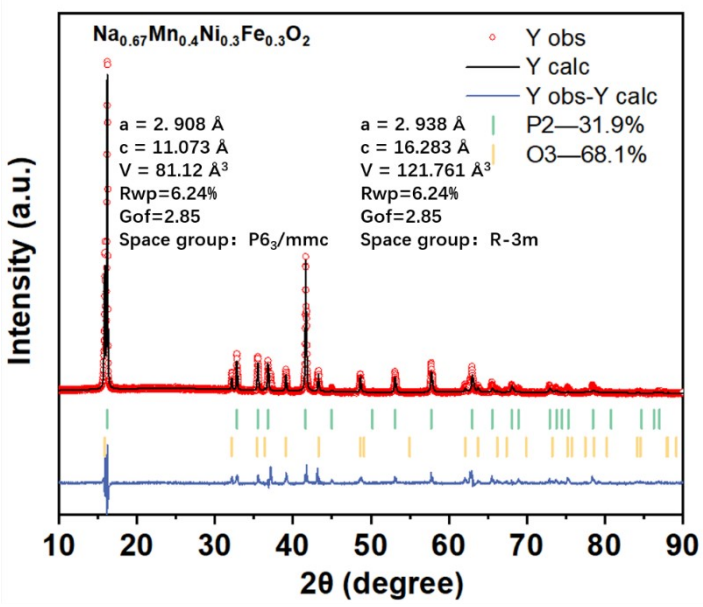

Fig. S6 XRD pattern and Rietveld refinement of $Na_{0.67}Mn_{0.4}Ni_{0.3}Fe_{0.3}O_2$.

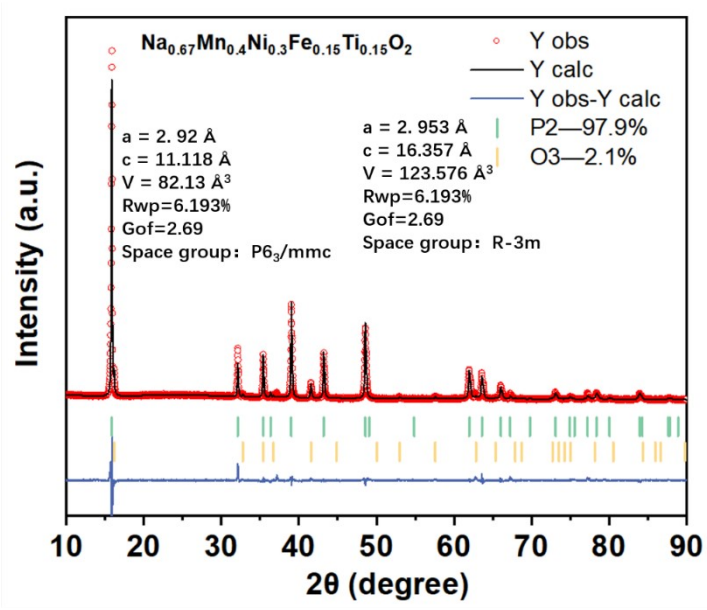

Fig. S7 XRD pattern and Rietveld refinement of $Na_{0.67}Mn_{0.4}Ni_{0.3}Fe_{0.15}Ti_{0.15}O_2$.

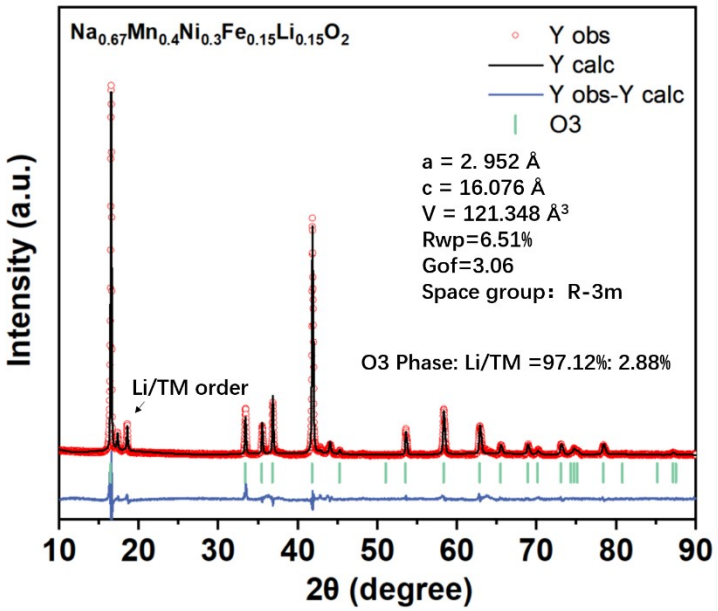

Fig. S8 XRD pattern and Rietveld refinement of $Na_{0.67}Mn_{0.4}Ni_{0.3}Fe_{0.15}Li_{0.15}O_2$.

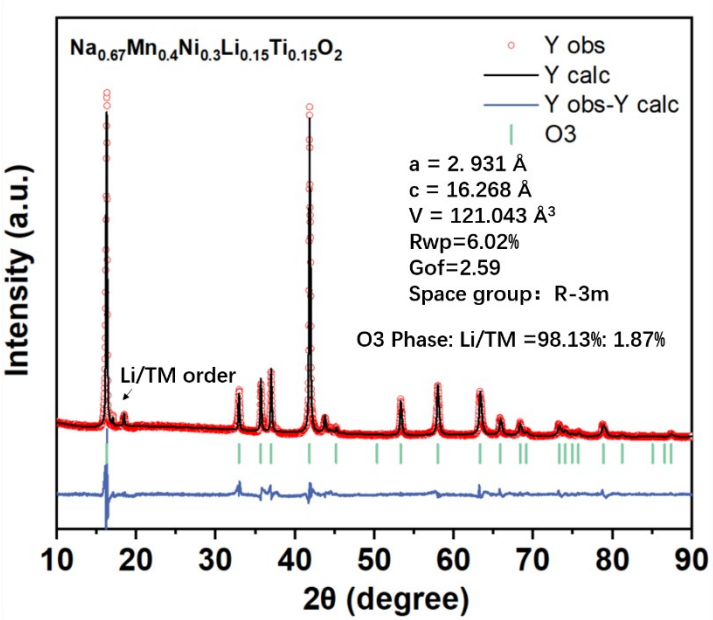

Fig. S9 XRD pattern and Rietveld refinement of $Na_{0.67}Mn_{0.4}Ni_{0.3}Li_{0.15}Ti_{0.15}O_2$.

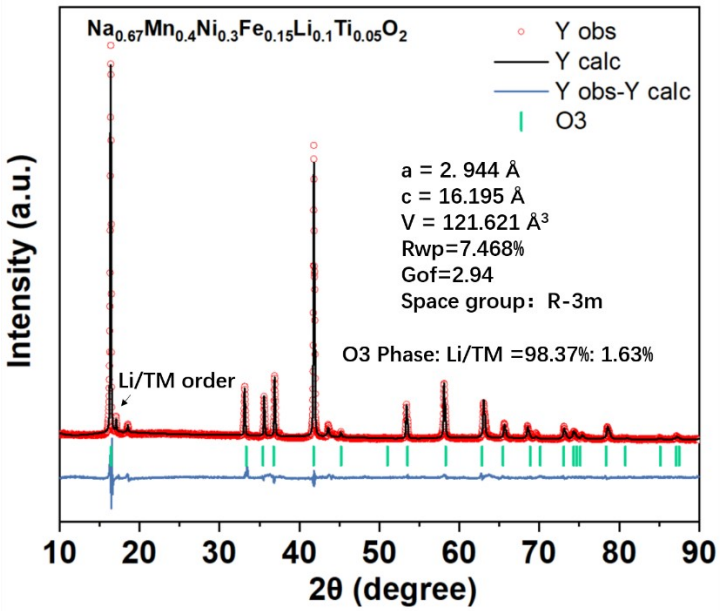

Fig. S10 XRD pattern and Rietveld refinement of $Na_{0.67}Mn_{0.4}Ni_{0.3}Fe_{0.15}Li_{0.1}Ti_{0.05}O_2$.

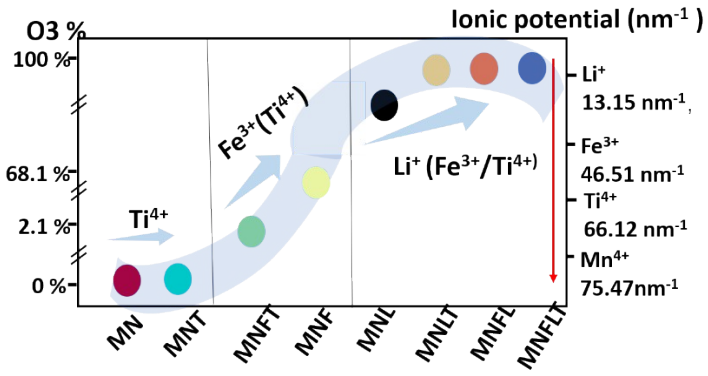

Fig. S11 O3 Structural ratios versus elemental ionic potentials. Taken together, the O3-promoting elements in the descending order is $Li^{+} > Fe^{3+} > Ti^{4+}$. The promoting effect is inversely proportional to the ionic potential energy. The good agreement indicates that the formation of material phases can be determined by fine-tuning the ionic potentials.

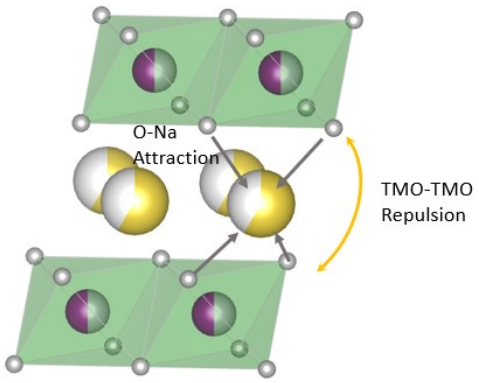

Fig. S12 Schematic illustration of the electrostatic interactions of off-stoichiometric O3.

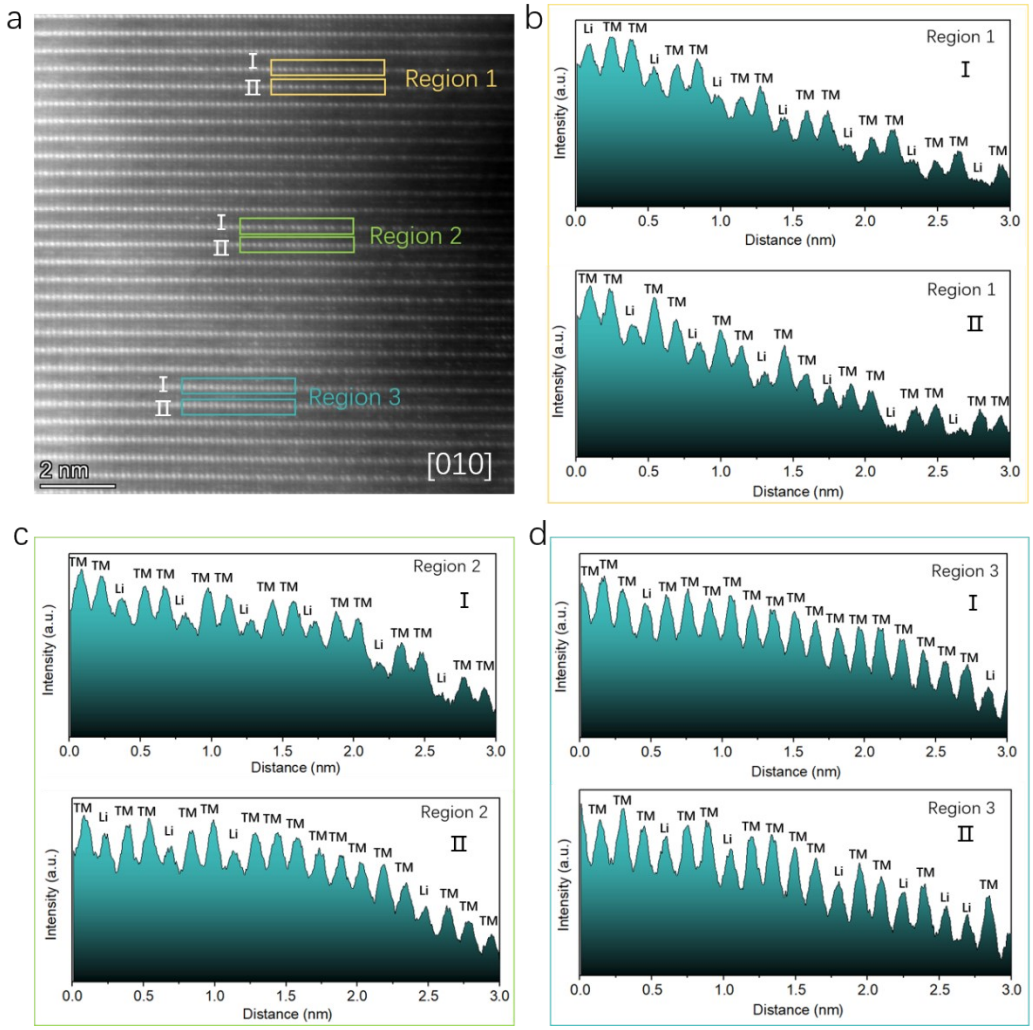

Fig. S13 HAADF–STEM image for a MNLT tests. The distribution of Li was categorized into three states, an ordered state of -TM-TM-Li- in region 1, a locally ordered state of Li/TM in region 2, and a disordered stochastic state of Li/TM in region 3. The superlattice peaks observed between 15° and 20° in the XRD are from the ordered Li/TM in region 1 and the locally ordered region of Li/TM in region 2.

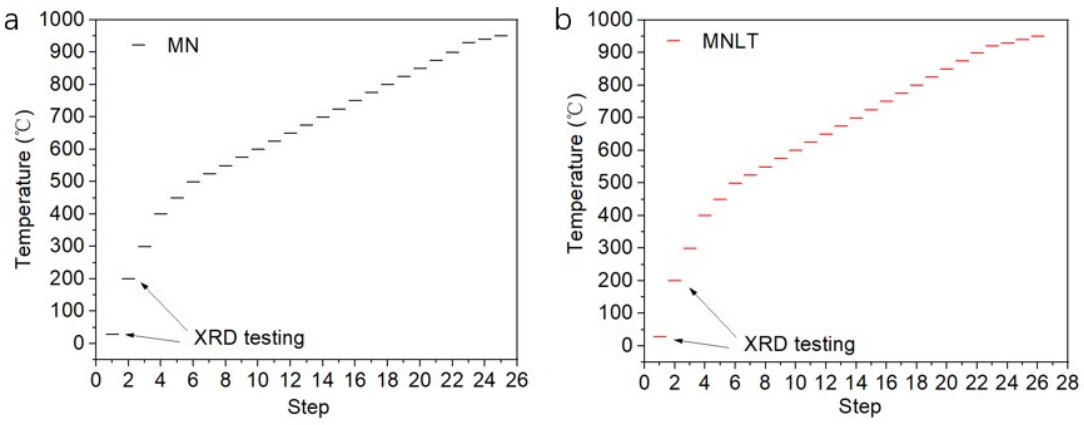

Fig. S14 Heat-up program for a) MN and b) MNLT tests.

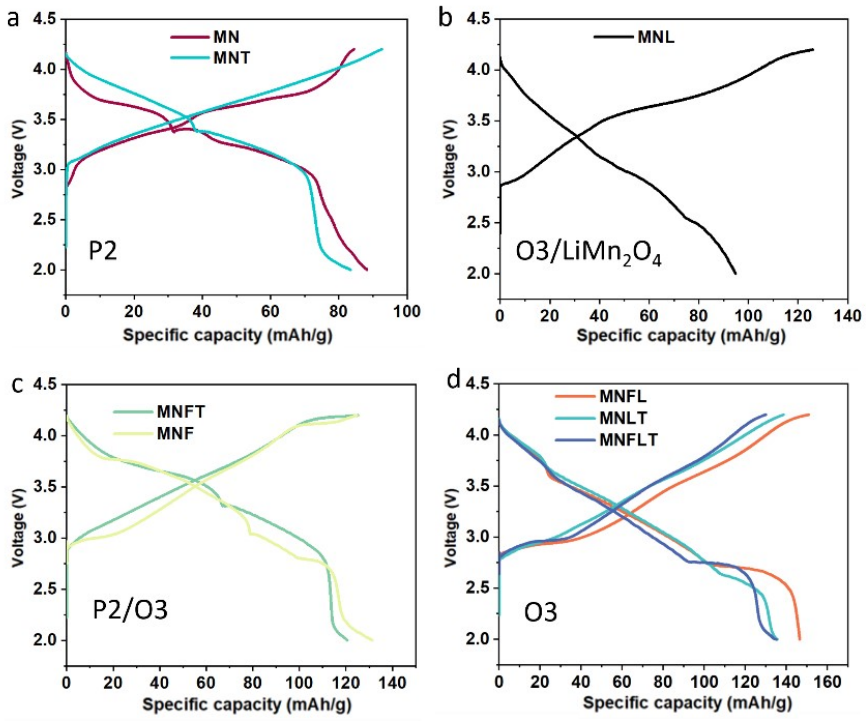

Fig. S15 The charging and discharging curves of $Na_{0.67}Mn_{0.7-x-y-z}Ni_{0.3}Li_xFe_yTi_zO_2$ series cathodes between 2-4.2V.

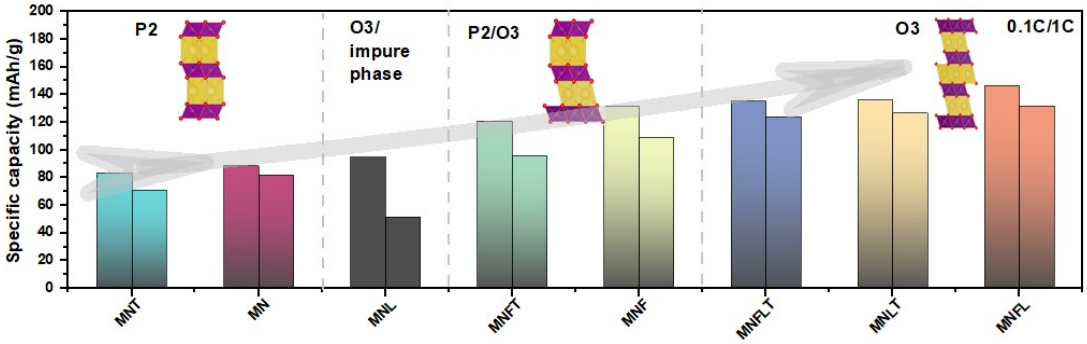

Fig. S16 The capacity of this series of cathodes at 0.1 C and 1 C rates.

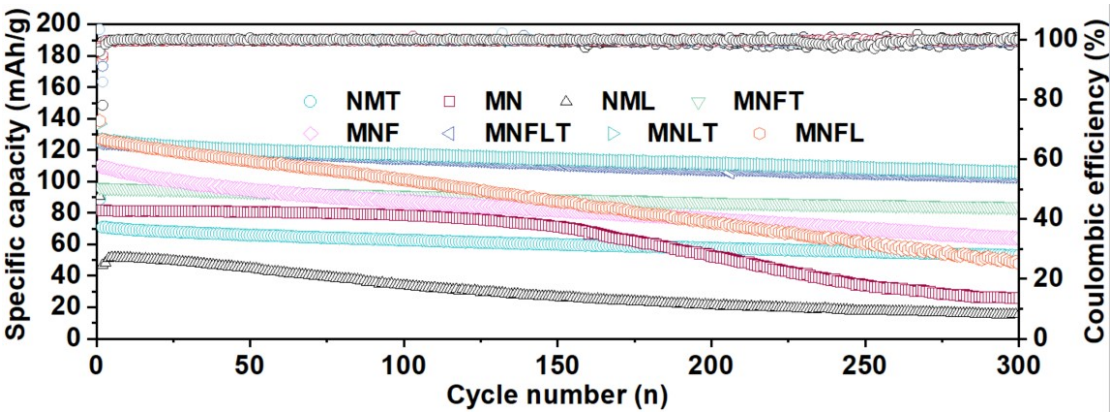

Fig. S17 Cycling performance of $Na_{0.67}Mn_{0.7-x-y-z}Ni_{0.3}Li_xFe_yTi_zO_2$ series cathodes at 1 C between 2-4.2 V. In the pure off-stoichiometric O3 series (MNLT, MNFL, MNFLT), the cycle stability of MNFL is not satisfactory (36.2%/300 cycles at 1C).

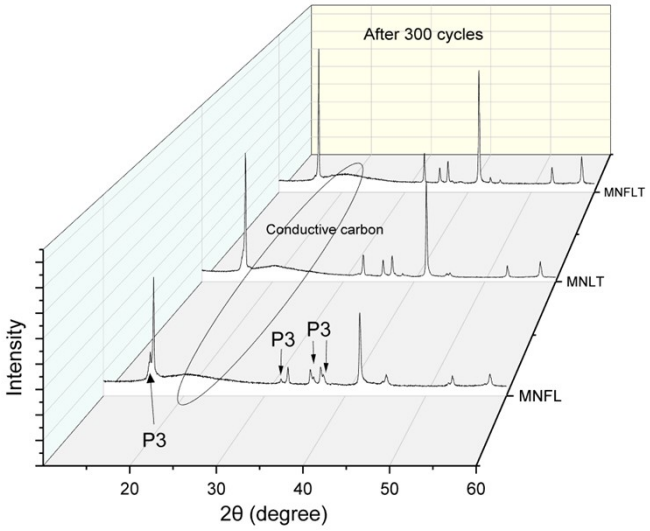

Fig. S18 XRD pattern of MNFLT, MNLT and MNFL after 300 cycles at 1C. Postmortem analysis of the electrodes of MNFL, MNLT, and MNFLT were conducted through XRD testing. MNLT and MNFLT retained their pristine O3 phase structures perfectly, while MNFL exhibited partial emergence of new P3 phase. Long cycling leads to irreversible phase transitions of O3 to P3, which is one of the significant reasons for capacity decay in O3 materials.

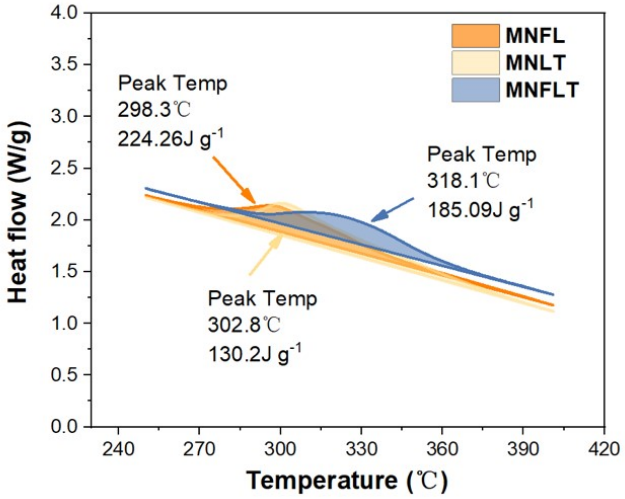

Fig. S19 Differential scanning calorimetry analysis of MNFL, MNLT and MNFLT cathodes in fully charged states (4.2 V). The fully charged (4.2 V) MNFL, MNLT, and MNFLT cathodes were further analyzed by DSC. The DSC curves of three desodiated cathodes exhibit pronounced exothermic peaks at ≈290– 320 °C, the heat energy released by the charged MNFL cathode is 224.26 J g^{-1} (at 298.3 °C), which is much higher than those released by the charged MNLT (130.2 J g^{-1} at 302.8 °C) and MNFLT (185.09 J g^{-1} at 318.1 °C). These results suggest that introducing strong Ti-O bonds in TM layer of off-stoichiometric O3 series can suppress structural degradation and thermal runaway.

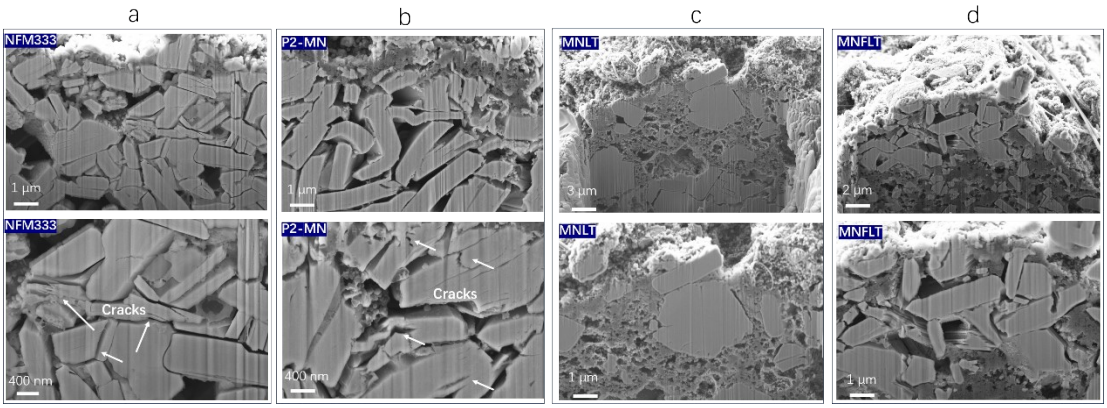

Fig. S20 Cross-sectional profiles of NFM333, P2-MN, MNLT and MNFLT after 300 cycles at 1 C rate. NFM333 and P2-MN show more microcracks.

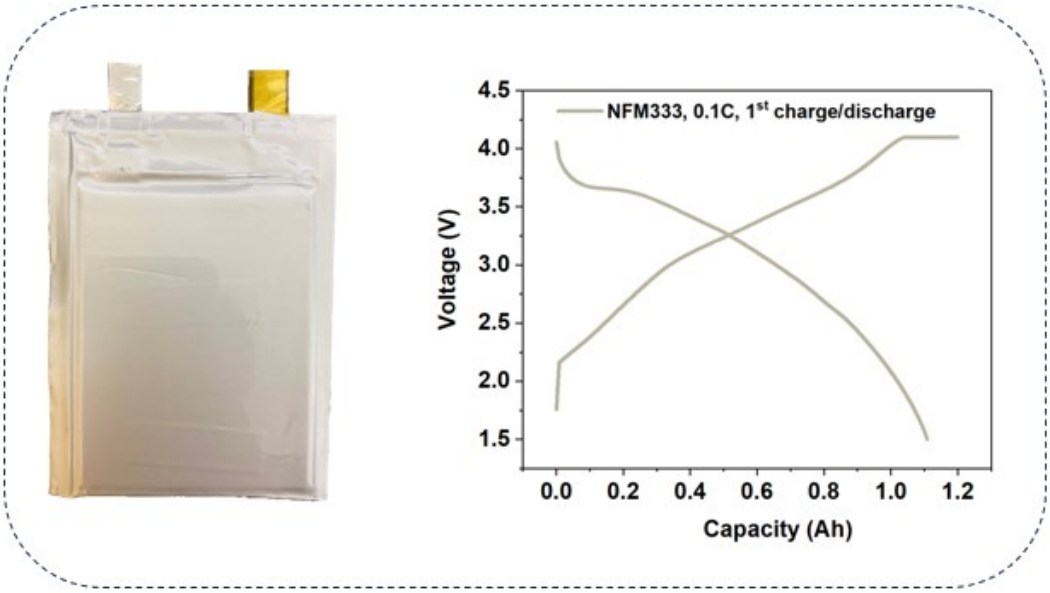

Fig. S21 NFM333 pouch cell (left) and first charge/discharge curve (right).

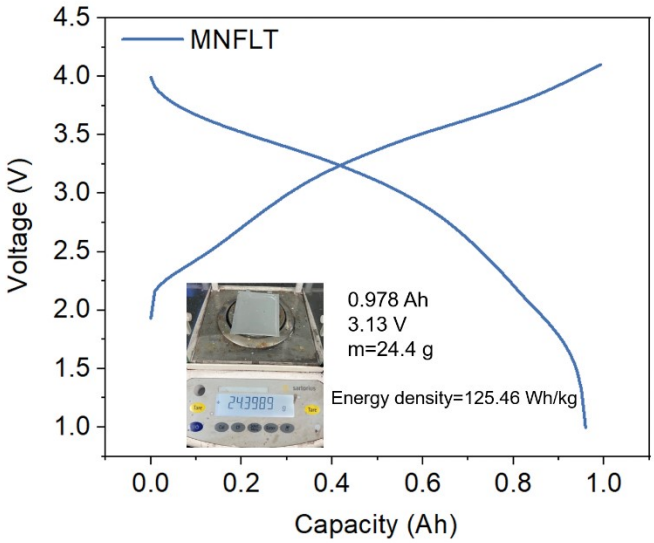

Fig. S22 MNFLT energy density. The comparison of MNFLT energy density with other reported cathodes has been presented in Table S3.

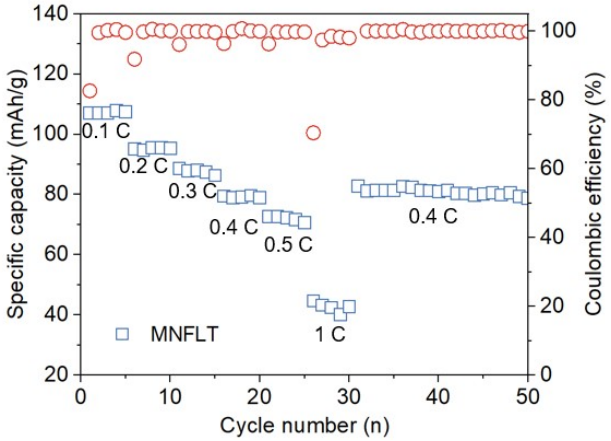

Fig. S23 Rate performance of MNFLT in solid-state batteries.

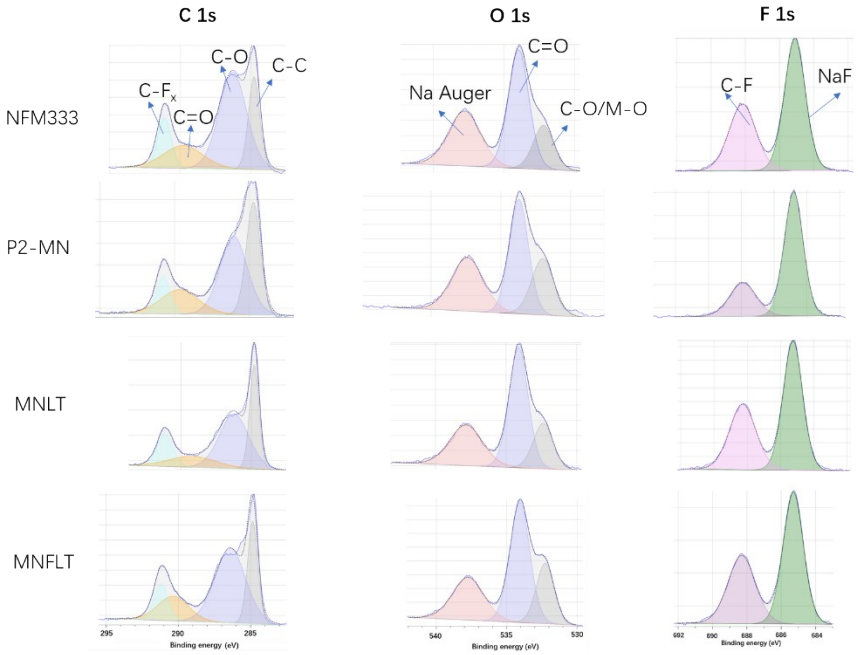

Fig. S24 NFM333, P2-MN, MNLT and MNFLT for 1 cycle between 2-4.2 V using 0.1 C rate to form CEI, and then examined the membrane components C, O, and F elements using XPS. The series of cathode membrane components and ratios are similar. Thereafter, the main focus is on information about the evolution of the phase structure.

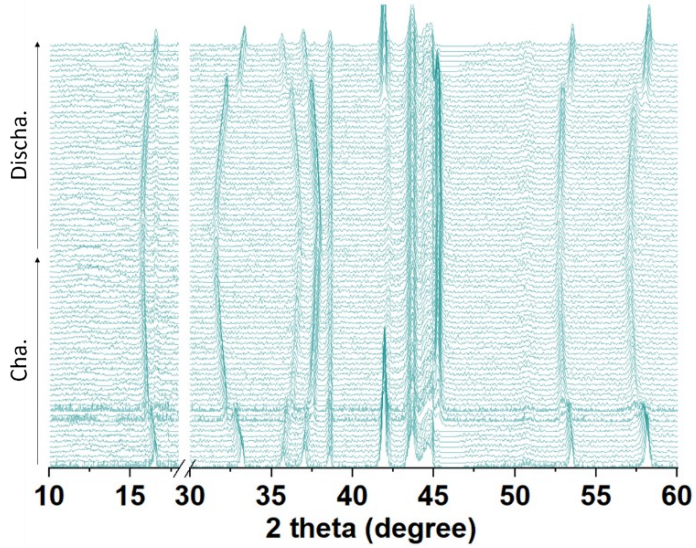

Fig. S25 In situ XRD patterns of MNFLT collected during the first charge/discharge at 0.2 C in the voltage range of 2–4.2 V.

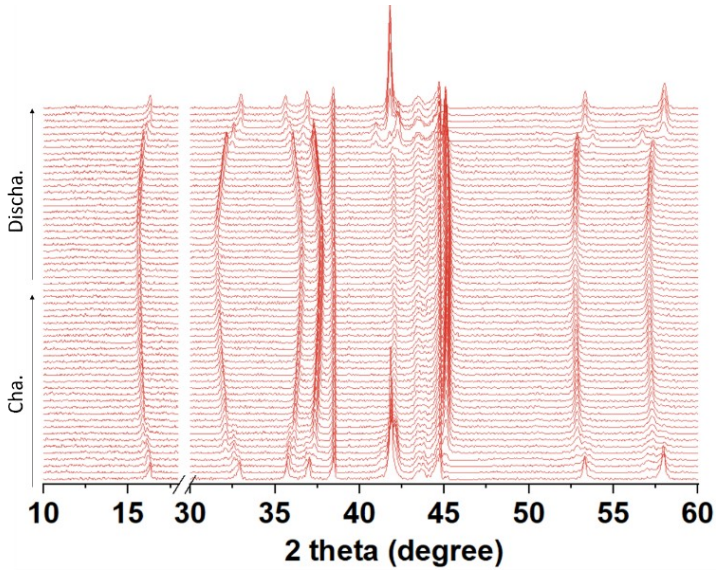

Fig. S26 In situ XRD patterns of MNLT collected during the first charge/discharge at 0.2 C in the voltage range of 2–4.2 V.

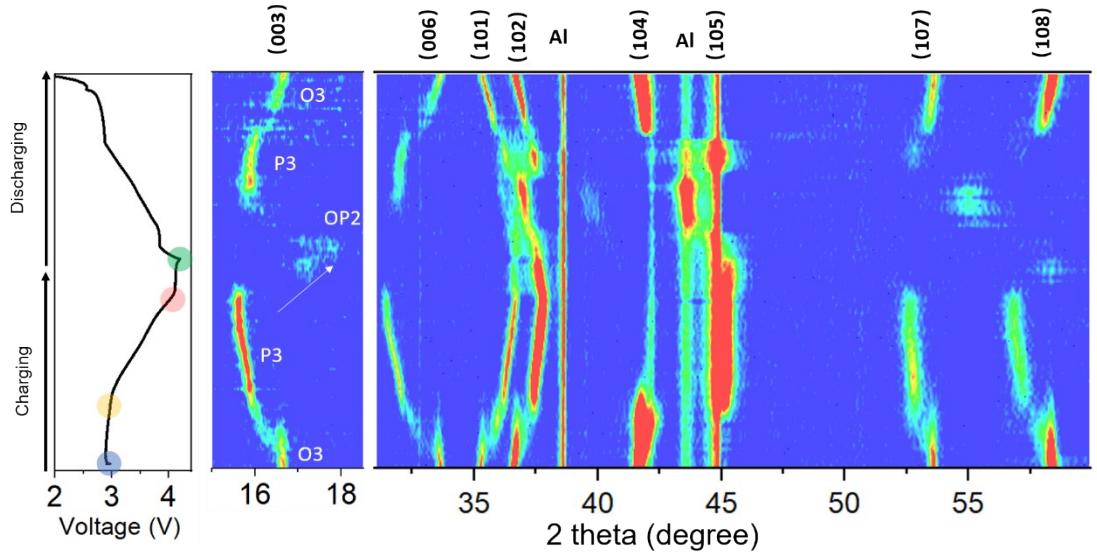

Fig. S27 2D contour plots of in-situ XRD during charge process of NFM333. NFM333 undergoes an O3-P3-OP2 phase transition between 2 and 4.2 V.

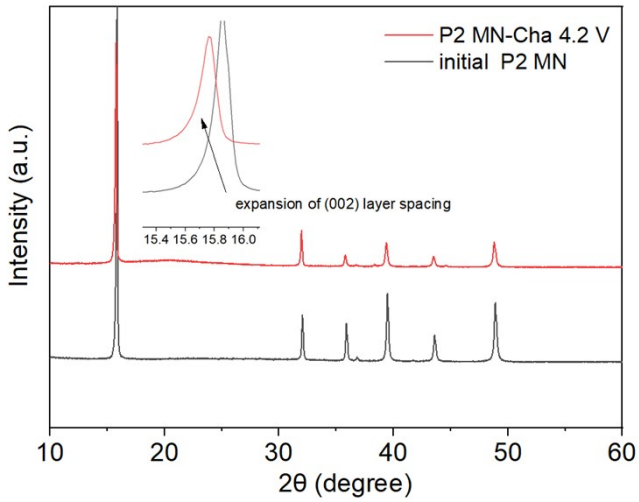

Fig. S28 XRD patterns of pristine MN and fully charged state MN (4.2V).

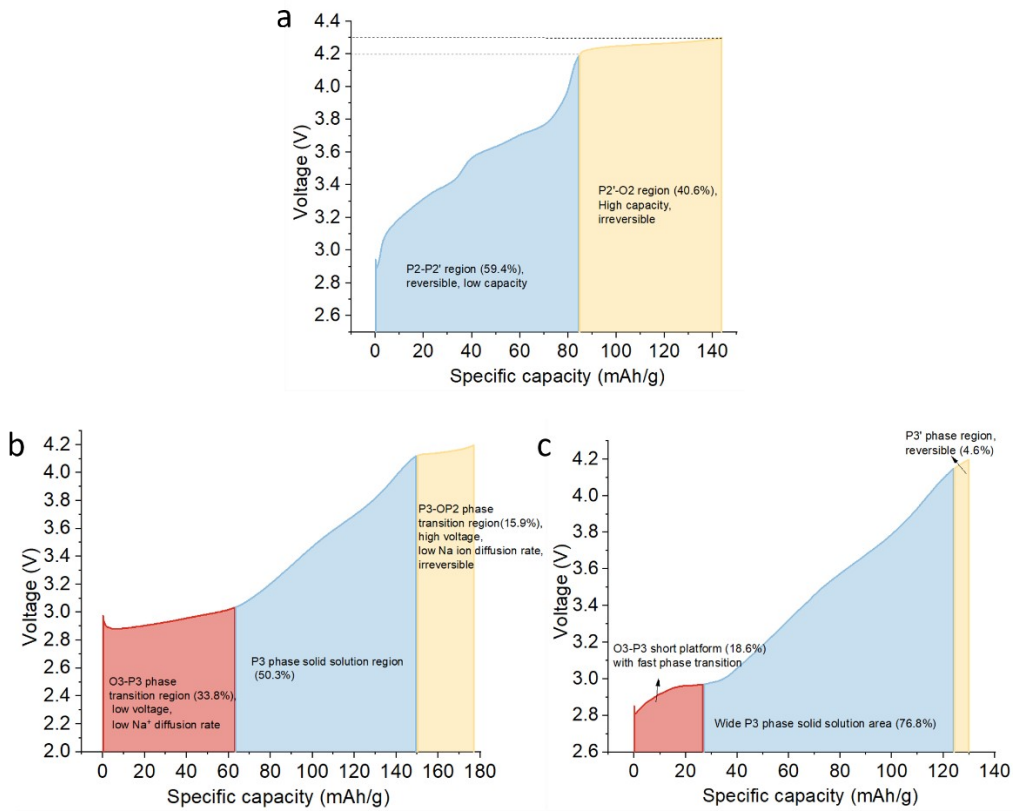

Fig. S29 a) MN capacity area distribution between 2-4.3V. b,c) NFM333 and MNFLT capacity area distribution between 2-4.2V.

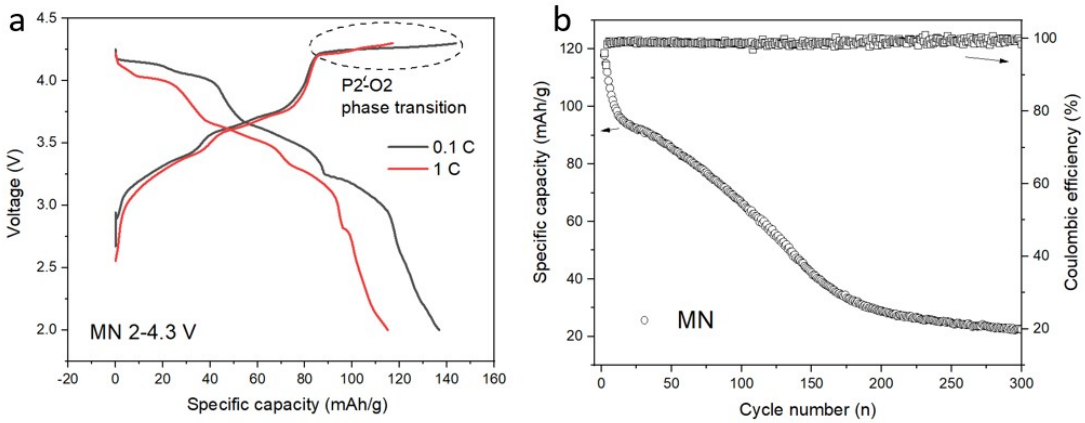

Fig. S30 a) MN charging and discharging curves and phase transition between 2-4.3V. b) Cycling stability at 1C rate.

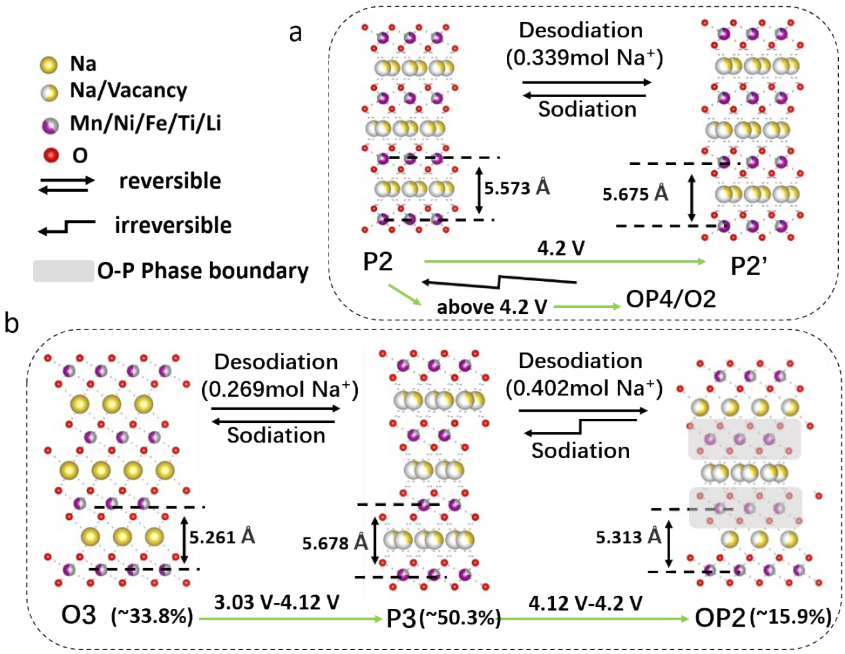

Fig. S31 Schematic view of structural changes and capacity partition for a) MN, b) NFM333 during Na (de)sodiation

Fig. S28-S31 summary: MN undergoes P2-P2' phase transition below 4.2V (**Fig. S28**), and the interslab distance of MN expands from 5.573 Å to 5.675 Å, with an expansion of 1.83%, this solid-solution phase transition provides a capacity of less than 90 mAh/g, further increasing the voltage to 4.3 V, the discharge capacity can reach 143.2 mAh/g at 0.1 C, but this part of capacity (about 40.6% of the overall capacity) comes from the irreversible P2'-O2 phase transition platform under high voltage (**Fig. S29**). This transition leads to a large volume change of 23%, and may be accompanied by anionic oxidation that destroys the layered structure, as evidenced that 300 cycles at 1C is only 16.7% of initial capacity **(Fig. S30)**. O3-NFM333 firstly undergoes the O3-P3 phase transition at low voltage ~3 V and is accompanied by an expansion of the interslab distance by 7.93% at the end of the P3 phase, followed by the P3-OP2 phase transition at 4.12 V-4.2 V, with a contraction of the interslab distance by 6.43%, which triggers a larger lattice mismatch prone to causing microcracks to form and expand, and reduces the structural integrity of the electrode.

In addition, the statistics of the capacity in terms of phase transition partitioning show that the O3-P3 and P3-OP2 phase transition platforms in NFM333 account for 33.8% and 15.9% of the total capacity, respectively, and the P-phase solid solution region only accounts for 50.3%. This representatively shows why the conventional O3 type materials have low discharge medium voltage, fast high voltage capacity decay and poor rate performance (**Fig. S31**).

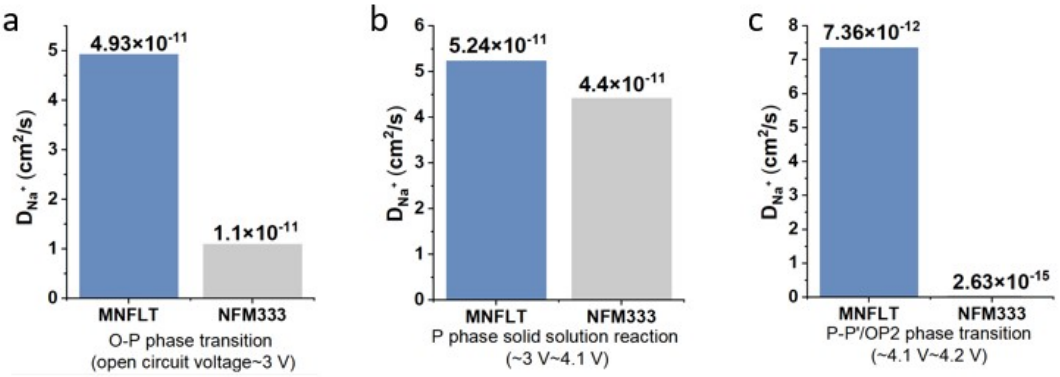

Fig. S32 Na^+ diffusion coefficients of MNFLT and NFM333 during the charge process.

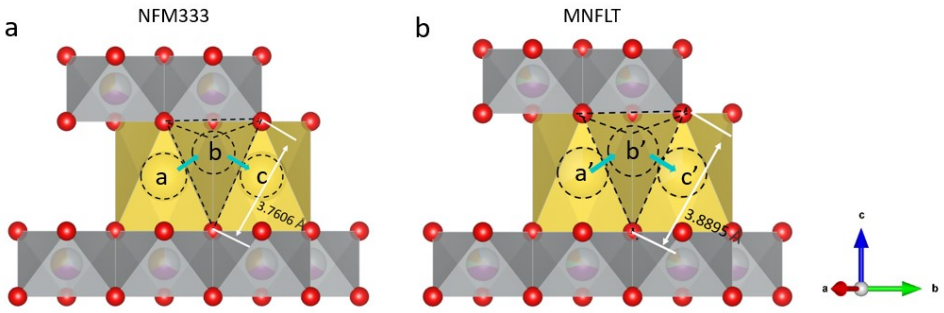

Fig. S33 Schematic illustration of Na^+ transport pathway and O-O intralayer distance of a) NFM333 and b) MNFLT.

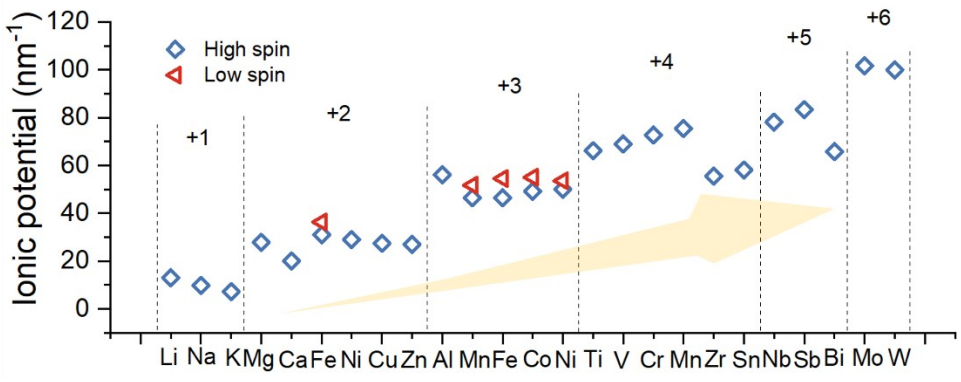

Fig. S34 Ionic potential of common battery elements.

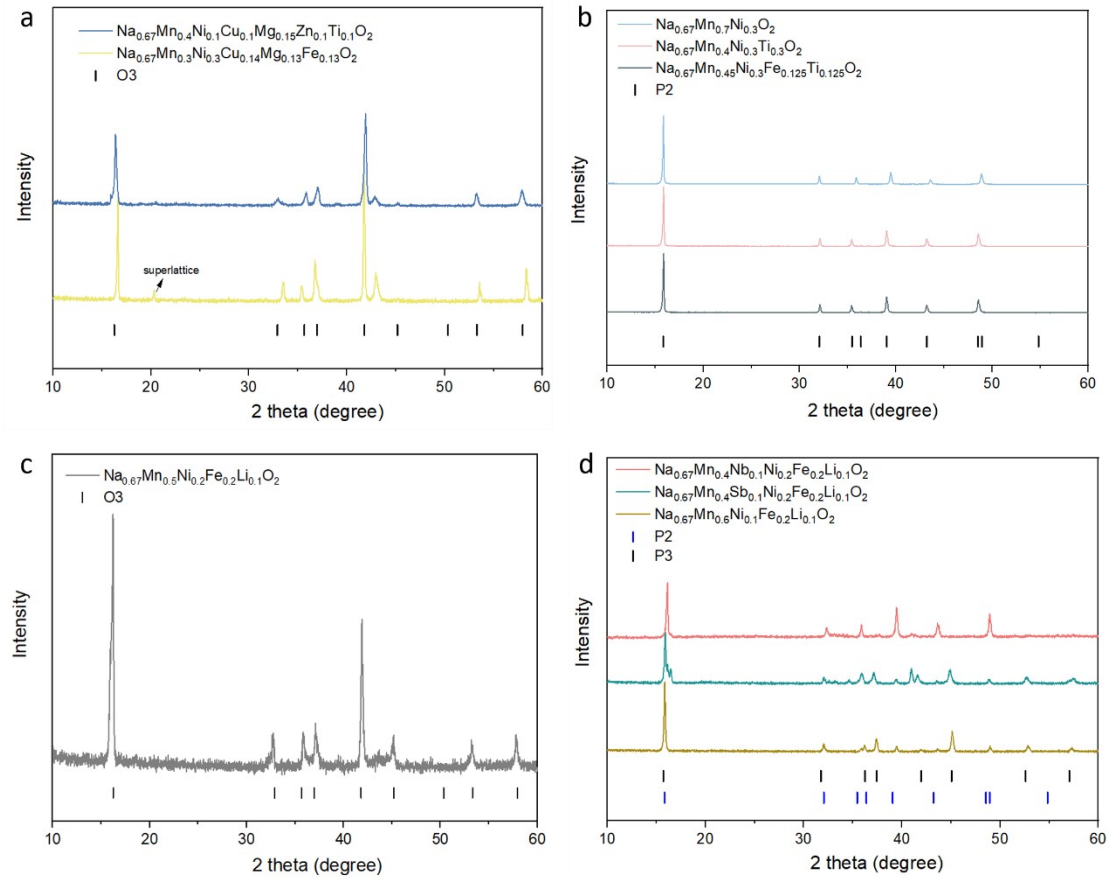

Fig. S35 a) Li-free doped O3 components. b) Li-free doped P2 components. c) Li doped O3 component. d) Li doped P2/P3 components. Sb^{5+} and Nb^{5+} doping to obtain mixed layered oxides of P2 and a small amount of P3 phases without any appearance of O3 phase.

The modulation and design of such off-stoichiometric NaO3 type materials are considered as follows. The study shows that Li^+ doping can promote the O3 type materials under high ionic potential, and the higher ionic potential tolerance encourages a wider range and ratio of optional TM layer elements. For example, the commonly used elements such as $Fe^{2+/3+}$, $Mn^{3+/4+}$, $Co^{2+/3+}$, $Ni^{2+/3+}$, Ti^{4+}, etc., which have moderately high ionic potential with their corresponding valence. The low Na conditions tend to generate P-phase or P/O mixed-phase structures when Li^+ is not added.

To obtain O3-type materials under low Na conditions, an excessive amount of lower ionic potential elements such as Mg^{2+}, Zn^{2+}, Cu^{2+}, etc. need to be introduced to ensure that the overall $\Phi < 12.296$, which often leads to a disproportionate ratio of active metals, reducing the cathode capacity, and also have the risk of precipitation of metal oxides.

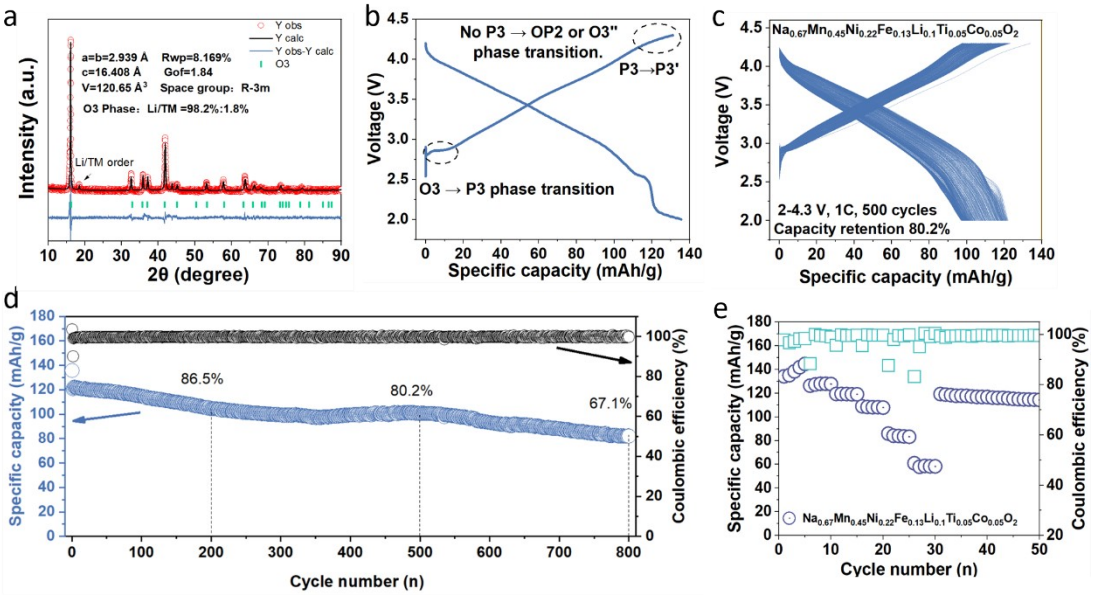

Fig. S36 a) XRD and Rietveld refinement results of $Na_{0.67}Mn_{0.45}Ni_{0.22}Fe_{0.13}Li_{0.1}Ti_{0.05}Co_{0.05}O_2$. b) Initial charge−discharge curves of $Na_{0.67}Mn_{0.45}Ni_{0.22}Fe_{0.13}Li_{0.1}Ti_{0.05}Co_{0.05}O_2$ at 0.1 C between 2-4.3 V (vs Na^+ /Na). c,d) Cycling stability of $Na_{0.67}Mn_{0.45}Ni_{0.22}Fe_{0.13}Li_{0.1}Ti_{0.05}Co_{0.05}O_2$.e) Rate performance of $Na_{0.67}Mn_{0.45}Ni_{0.22}Fe_{0.13}Li_{0.1}Ti_{0.05}Co_{0.05}O_2$.

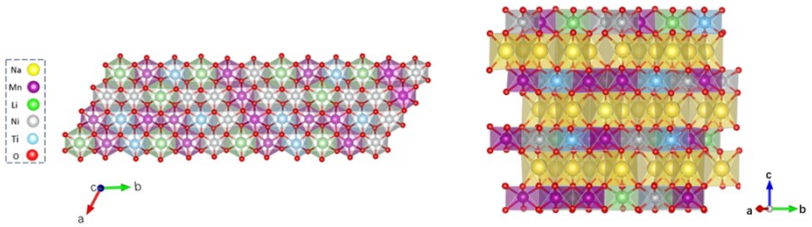

Fig S37 Na^+ in MNLT are finally stabilized at the octahedral position.

References

1. J. Fu, S. Wang, D. Wu, J. Luo, C. Wang, J. Liang, X. Lin, Y. Hu, S. Zhang, F. Zhao, W. Li, M. Li, H. Duan, Y. Zhao, M. Gu, T.-K. Sham, Y. Mo and X. Sun, *Advanced Materials*, 2024, **36**, 2308012.
2. G. Kresse and J. Furthmüller, *Computational Materials Science*, 1996, **6**, 15-50.
3. V. I. Anisimov, J. Zaanen and O. K. Andersen, *Physical Review B*, 1991, **44**, 943-954.
4. C. Zhao, Q. Wang, Z. Yao, J. Wang, B. Sánchez-Lengeling, F. Ding, X. Qi, Y. Lu, X. Bai, B. Li, H. Li, A. Aspuru-Guzik, X. Huang, C. Delmas, M. Wagemaker, L. Chen and Y.-S. Hu, *Science*, 2020, **370**, 708-711.
5. L. Bordet-Le Guenne, P. Deniard, P. Biensan, C. Siret and R. Brec, *Journal of Materials Chemistry*, 2000, **10**, 2201-2206.
6. Y. Ono, N. Kato, Y. Ishii, Y. Miyazaki, T. J. J. o. t. J. S. o. P. Kajitani and P. Metallurgy, *Journal of the Japan Society of Powder and Powder Metallurgy*, 2003, **50**, 469-474.
7. J. M. Paulsen, R. A. Donaberger and J. R. Dahn, *Chemistry of Materials*, 2000, **12**, 2257-2267.
8. T. Zhou, D. Zhang, T. W. Button, F. J. Berry and C. Greaves, *Dalton Transactions*, 2010, **39**, 1089-1094.
9. O. A. Smirnova, M. Avdeev, V. B. Nalbandyan, V. V. Kharton and F. M. B. Marques, *Materials Research Bulletin*, 2006, **41**, 1056-1062.
10. Y.-J. Shin and M.-Y. J. S. S. I. Yi, *Solid State Ionics*, 2000, **132**, 131-141.
11. Y.-J. Shin, M.-H. Park, J.-H. Kwak, H. Namgoong and O. H. J. S. S. I. Han, *Solid State Ionics*, 2002, **150**, 363-372.
12. G. Shilov, V. Nalbandyan, V. Volochaev and L. J. I. J. o. I. M. Atovmyan, *International Journal of Inorganic Materials*, 2000, **2**, 443-449.
13. J. S. Thorne, R. A. Dunlap and M. N. Obrovac, *Journal of The Electrochemical Society*, 2014, **161**, A2232.
14. H. Yoshida, N. Yabuuchi and S. Komaba, *Electrochemistry Communications*, 2013, **34**, 60-63.
15. S. J. Clarke, A. J. Fowkes, A. Harrison, R. M. Ibberson and M. J. Rosseinsky, *Chemistry of Materials*, 1998, **10**, 372-384.
16. W. Scheld and R. Hoppe, *Zeitschrift für anorganische und allgemeine Chemie*, 1989, **568**, 151-156.
17. H. Watanabe and M. Fukase, *Journal of the Physical Society of Japan*, 1961, **16**, 1181-1184.
18. C. Fouassier, G. Matejka, J.-M. Reau and P. J. J. o. S. S. C. Hagenmuller, *Journal of Solid State Chemistry*, 1973, **6**, 532-537.
19. J. Bréger, K. Kang, J. Cabana, G. Ceder and C. P. Grey, *Journal of Materials Chemistry*, 2007, **17**, 3167-3174.
20. P. Vassilaras, A. J. Toumar and G. J. E. c. Ceder, *Electrochemistry Communications*, 2014, **38**, 79-81.
21. S.-M. Oh, S.-T. Myung, C. S. Yoon, J. Lu, J. Hassoun, B. Scrosati, K. Amine and Y.-K. Sun, *Nano Letters*, 2014, **14**, 1620-1626.
22. C. Zhao, M. Avdeev, L. Chen and Y.-S. Hu, *Angewandte Chemie International Edition*, 2018, **57**, 7056-7060.

23. Y. Tang, Q. Zhang, W. Zuo, S. Zhou, G. Zeng, B. Zhang, H. Zhang, Z. Huang, L. Zheng, J. Xu, W. Yin, Y. Qiu, Y. Xiao, Q. Zhang, T. Zhao, H.-G. Liao, I. Hwang, C.-J. Sun, K. Amine, Q. Wang, Y. Sun, G.-L. Xu, L. Gu, Y. Qiao and S.-G. Sun, *Nature Sustainability*, 2024, **7**, 348-359.
24. X. Wang, Q. Zhang, C. Zhao, H. Li, B. Zhang, G. Zeng, Y. Tang, Z. Huang, I. Hwang, H. Zhang, S. Zhou, Y. Qiu, Y. Xiao, J. Cabana, C.-J. Sun, K. Amine, Y. Sun, Q. Wang, G.-L. Xu, L. Gu, Y. Qiao and S.-G. Sun, *Nature Energy*, 2024, **9**, 184-196.
25. S. Gao, Z. Zhu, H. Fang, K. Feng, J. Zhong, M. Hou, Y. Guo, F. Li, W. Zhang and Z. J. A. M. Ma, *Advanced Materials*, 2024, **36**, 2311523.
26. T. Zhang, M. Ren, Y. Huang, F. Li, W. Hua, S. Indris and F. Li, *Angewandte Chemie International Edition*, 2024, **63**, e202316949.
27. V. K. Kumar, S. Ghosh, S. Biswas and S. K. Martha, *Journal of The Electrochemical Society*, 2020, **167**, 080531.
28. M. Li, H. Zhuo, M. Song, Y. Gu, X. Yang, C. Li, Z. Liao, Y. Ye, C. Zhao and Y. J. N. E. Jiang, *Nano Energy*, 2024, **123**, 109375.